THE JOURNAL OF PHYSICAL CHEMISTRY C

Article

pubs.acs.org/JPCC

Visualization of the Phase Propagation within Carbon-Free $Li_4Ti_5O_{12}$ Battery Electrodes

Chunjoong Kim,[†,‡,§,∥] Young-Sang Yu,[†,‡,∥,⊥] Benjamin Moyon,[‡] Chutchamon Sirisopanaporn,[‡] Thomas J. Richardson,[‡] and Jordi Cabana*[,†,‡]

[†]Department of Chemistry, University of Illinois at Chicago, Chicago, Illinois 60607, United States

[‡]Environmental Energy Technologies Division, Lawrence Berkeley National Laboratory, Berkeley, California 94720, United States

Supporting Information

ABSTRACT: The electrochemical reactions occurring in batteries involve the transport of ions and electrons among the electrodes, the electrolyte, and the current collector. In Li-ion battery electrodes, this dual functionality is attained with porous composite electrode structures that contain electronically conductive additives. Recently, the ability to extensively cycle composite electrodes of $Li_4Ti_5O_{12}$ without any conductive additives generated questions about how these structures operate, the answers to which could be used to design architectures with other materials that reduce the amount of additives that do not directly store energy. Here, the changes occurring in carbon-free $Li_4Ti_5O_{12}$ electrodes during lithiation were studied by a combination of ex situ and operando optical microscopy and microbeam X-ray absorption spectroscopy (μ-XAS). The measurements provide visualizations of the percolation of lithiated domains through the thick (~40-μm) structure after a depth of discharge of only 1%, followed by a second wave of propagation starting with regions in closest contact with the current collector and progressing toward regions in contact with the bulk electrode. These results emphasize the interplay between the electronic and ionic conductivities of the phases involved in a battery reaction and the formation of the phases in localized areas in the electrode architecture. They provide new insights that could be used to refine the design of these architectures to minimize transport limitations while maximizing energy density.

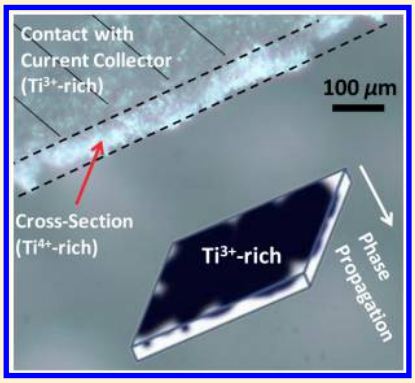

1. INTRODUCTION

Li-ion batteries are the most important energy storage devices today because of their high energy/power density, negligible memory effects, low self-discharge properties, and long lives.[1−3] They are currently under close scrutiny as storage systems for a renewable energy-based electricity grid and have an incipient presence in the market of electric vehicles, boosted by growing concerns over the finite supply and environmental consequences of fossil fuels. Still, breakthroughs must be achieved to implement Li-ion batteries in these applications at the required scales.[4−6] As a result, intensive research efforts have been devoted to finding better materials and designing architectures to improve the performance of those currently being used.[7−10] Battery electrodes are currently built in the form of a 50−100-μm-thick porous composite of a redox-active material, a conductive additive, and a polymeric binder to ensure the dual transport of electrons and ions required to complete an electrochemical reaction.[11] Component assembly during the formation of these composites is poorly controlled, resulting in architectures that, although cheap, quick, and efficient to build, handicap the inherent performance of the active material[12] and require postfabrication procedures of quality control that add overhead in time and costs.[13] Achieving full control of the fabrication of electrodes requires understanding how materials function at the electrode level, where kinetic conditions always prevail, in comparison with ideal, even close-to-equilibrium conditions of cycling.

The energy density of a battery can be raised by increasing the mass loading of active material per unit area in the electrode, for instance, by reducing the ratio of support components.[14] However, when poorly electronically conducting materials are used as electrodes, performance losses are predicted if the corresponding additives are removed, particularly if the electrode material is a wide-band-gap semiconductor. Examples are titanium(IV) oxides, which are highly electronically insulating because they have empty 3d orbitals. Phases such as the different TiO_2 polytypes, $Li_2Ti_3O_7$, and especially $Li_4Ti_5O_{12}$ are alternatives to graphitic carbonaceous materials that provide comparatively higher rate capabilities and safety when used as negative electrodes.[15−17] $Li_4Ti_5O_{12}$ is considered to be a good choice for the negative electrode in applications where power and durability are critical. It has classically been considered to react with Li^+ through a two-phase reaction to produce $Li_7Ti_5O_{12}$ at ~1.55 V vs Li^+/Li^0, for a theoretical specific capacity of 175 mAh g^{-1}, because of the prominent plateau of potential observed during the electrochemical reaction.[18,19] However, recent work suggests

Received: November 14, 2016
Revised: November 23, 2016
Published: November 28, 2016

DOI: 10.1021/acs.jpcc.6b11459
J. Phys. Chem. C 2016, 120, 29030−29038

that segregation of domains of different lithium concentrations occurs at such a short scale (less than 10 nm)[20] that complete mixing into pure solid solutions is possible under certain conditions.[21,22] In any case, the negligible volume change ($\Delta V \approx 0.2\%$) induced between the two end phases brings about excellent cycling stability and rate performance.[18,19]

So far, the poor conductive properties of $Li_4Ti_5O_{12}$ in the pristine state have led researchers to focus on synthesizing or processing it in composites with carbon to ensure good performance.[23,24] However, recent work has demonstrated that $Li_4Ti_5O_{12}$,[25−27] as well as other titanium oxides,[28,29] can be made to cycle very stably without conducting agents in the composite electrode. The key to this behavior is the rapid propagation of lithiated domains throughout the composite structure. These domains both contain mixed Ti^{3+}/Ti^{4+} (d^1/d^0) states, which create electronic carriers,[27] and show enhanced Li diffusion with respect to the initial state.[30] Percolation of these domains throughout the electrode architecture at very low overall levels of lithiation creates a conductive network in situ, inducing a sharp increase in electronic conductivity that enables the reaction to complete lithiation.[27] The occurrence of percolation was inferred from the detection by Raman spectroscopy of electronically conducting states in the top layers of the electrode, away from the current collector, as well as a sharp drop in the electrical impedance of the electrode. Recently, conductive scanning probe measurements refined this insight by noting that the electronically conducting states at the surface of a thin (<1-μm) film were not laterally homogeneous but, rather, formed percolation "channels".[31] However, the propagation of lithiated domains in a real, thick composite electrode has not yet been visualized.

Analytical tools exist to detect compositional or structural changes at various length scales, using X-ray, laser, or visible radiation.[32−35] Optical microscopy is ideally suited for an electrode system containing titanium oxides,[36] because the color of the active phase changes from white to dark blue upon lithiation.[26,27] However, optical microscopy offers only qualitative information, and thus, the relative ratios of the species cannot be quantified. In contrast, X-ray absorption spectroscopy (XAS) can directly provide electronic signatures, by which oxidation states and local coordination can be obtained without the need for the domains to be crystalline. Thus, raster scans of focused hard X-ray microbeams combined with energy tunability across the K-edge absorption of transition metals (i.e., microbeam X-ray absorption spectroscopy, μ-XAS) constitute an ideal means for quantitatively visualizing, at high resolution, chemical compositional maps for electrodes at intermediate states of charge.[37−39]

In this study, we visualized the electrochemical lithiation of $Li_4Ti_5O_{12}$ in composite electrodes free of conductive additives, primarily in cell configurations in which the electron and ion supplies (from the current collector and bulk electrolyte, respectively) were located on opposite sides. The phase front was traced by ex situ and operando optical microscopy measurements by leveraging the large color contrast between end phases, whereas composition was quantitatively determined by using μ-XAS across the titanium K-edge. As a result, the propagation of lithiated domains that we proposed in an earlier report was confirmed,[26] and lateral compositional domains were identified, likely as being due to inhomogeneities in the distributions of active material, binder, and pores in the composite electrode.

2. EXPERIMENTAL SECTION

2.1. Material Synthesis. $Li_4Ti_5O_{12}$ was synthesized by a solid-state reaction using Li_2CO_3 (Sigma-Aldrich, no. 62470) and anatase TiO_2 (Sigma-Aldrich, no. 248576) as starting materials, mixed in a stoichiometric ratio in a mortar, followed by annealing at 850 °C for 5 h under ambient atmosphere. The cooling rate was set to 2 °C min^{-1}.

2.2. Characterization. Powder X-ray diffraction (XRD) was performed on a D2 Phaser (Bruker AXS) diffractometer equipped with Cu Kα radiation (λ_{avg} = 1.5418 Å). Scanning electron microscopy (SEM) images were obtained with a JEOL JSM-7500F field-emission microscope in gentle beam mode at 1 kV and 20 mA. High-resolution digital optical microscopy was carried out on a MXG-2500REZ microscope (Hirox Co., Ltd.) at magnifications ranging from 35× to 2500×. X-ray absorption spectroscopy was carried out at the Ti K-edge at beamline 2-3 of the Stanford Synchrotron Radiation Lightsource (SSRL) at the SLAC National Accelerator Laboratory (Stanford, CA). This beamline is equipped with Kirkpatrick−Baez (K−B) optics that were used to focus the beam to an area of 2 × 2 μm^2. To obtain the pixel-by-pixel fluorescence yield, the focused beam was raster scanned onto a 500 × 500 μm^2 field of view with a 45° incidence angle. All single-pixel fluorescence yields and X-ray absorption spectra were simultaneously collected with a Vortex fluorescence detector and an ionization chamber as the incident X-ray energy was tuned across the Ti K-edge.[40] Four fluorescence yield maps were collected at characteristic fluorescence features (at 4971, 4976, and 4987 eV) that have clear contrasts corresponding to the oxidation states of Ti and the postedge region (5017 eV) for normalization. The intensity of the incident X-ray was normalized using the flux measured in the first ionization chamber positioned between the sample and the source. Because the fluorescence yield in the postedge region is not affected by the oxidation states of Ti, the other fluorescence maps were normalized to the map at 5017 eV to regularize the fluorescence yields with respect to variations in the sample (e.g., sample thickness). To obtain the chemical phase distribution of the sample with a 50% depth of discharge (DOD, which is the percentage of battery capacity that has been discharged expressed as a percentage of the maximum specific capacity), least-squares linear-combination (LC) fitting with normalized standard spectra of $Li_4Ti_5O_{12}$ and $Li_7Ti_5O_{12}$ was performed for each single-pixel fluorescence yield. To enhance the visibility, the color scale of the chemical map was limited to the range of 9.4−11.4% of DOD. To confirm the accuracy of the chemical map, the full spectra were also measured at the most oxidized and most reduced single pixels (Figure S1 of the Supporting Information), which resulted in compositions equivalent to ∼9.4% DOD (corresponding to $Li_{\sim 4.28}Ti_5O_{12}$) and ∼11.4% DOD ($Li_{\sim 4.34}Ti_5O_{12}$), respectively. The quality of LC fit for the full spectra (Figure S1, Supporting Information) was confirmed by means of the R factor, defined as $R = \sum(\text{data} - \text{fit})^2/\sum(\text{data})^2$. All data processing, including normalization of fluorescence spectra and LC fitting, was performed using SIXPack[41] and the SMAK MicroAnalysis Toolkit.[42] All cell assembly and sample manipulation was performed in an Ar-filled glovebox, and the ex situ samples for μ-XAS measurements were sealed in Mylar 400 (Dupont, 50-μm-thick polyester films) to protect them from deleterious contact with the ambient atmosphere.

DOI: 10.1021/acs.jpcc.6b11459
J. Phys. Chem. C 2016, 120, 29030−29038

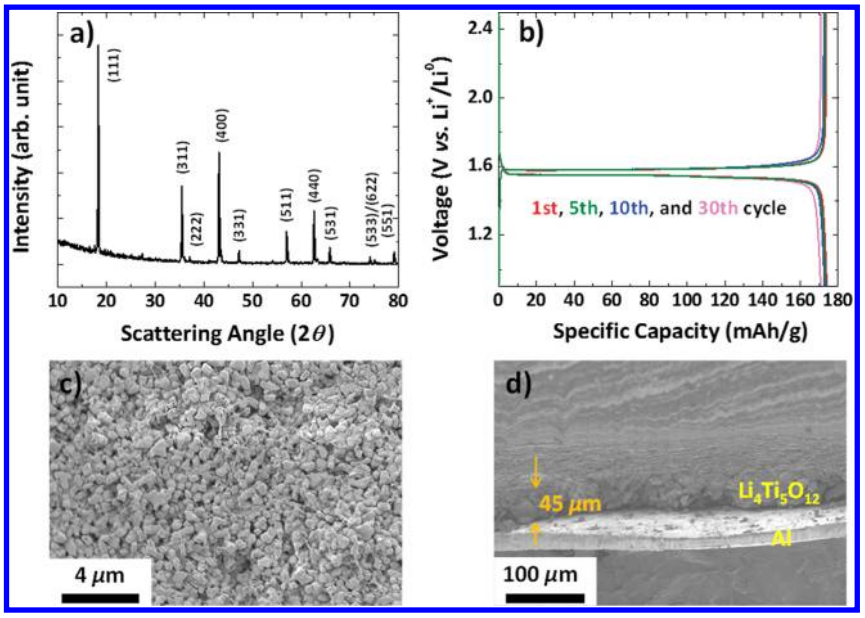

Figure 1. (a) XRD pattern of $Li_4Ti_5O_{12}$. (b) Voltage−capacity curve of carbon-free $Li_4Ti_5O_{12}$ electrodes, cycled in Li metal half-cells at a rate of C/10. (c,d) SEM images of the composite electrodes (c) in the plane and (d) along their cross section.

2.3. Electrode Preparation and Evaluation of Electrochemical Properties. The working electrodes were prepared by mixing $Li_4Ti_5O_{12}$ and poly(vinylidene difluoride) (PVDF) in *N*-methyl pyrrolidone (NMP) in a mass ratio of 90:10. When homogeneity was reached, the slurry was cast onto aluminum foil and then dried under a vacuum at 110 °C overnight. The dried electrodes had an areal loading of ~8.4 g cm^{-2} and were calendered with a line pressure of 600 kgf cm^{-1} with a roll press (IRM Lab Mill Table model). The calendered electrodes were ~45 μm thick, which corresponds to ~40% porosity. Electrodes were punched into disks with a diameter of $^3/_8$ in. and transferred to an Ar-filled glovebox (≤0.1 ppm of both water and oxygen). 2032-type coin cells were assembled with $Li_4Ti_5O_{12}$, high-purity lithium foil (Sigma-Aldrich, no. 320080), and Celgard 2500 as working electrodes, counter electrodes, and separators, respectively. The electrolyte was composed of 1 M $LiPF_6$ in a mixture of ethylene carbonate (EC) and diethyl carbonate (DEC) in a volume ratio of 50:50 (Novolyte Technologies). Charge−discharge measurements of $Li_4Ti_5O_{12}$ vs Li^+/Li^0 were recorded on a Biologic VMP3 potentiostat at room temperature at a C/10 rate between 0.9 and 2.5 V, where C = 175 mA g^{-1} corresponds to the current needed to reach the theoretical capacity of the electrode in 1 h. Ex situ samples for optical microscopy studies were carefully harvested from cells at the desired DOD states in the Ar-filled glovebox and placed in the airtight sealed sample stage. Samples with 0, 1, 10, 25, 50, 75, and 100% DOD were prepared, which corresponded to discharge capacities of 0, 1.75, 17.5, 43.75, 87.5, 131.25, and 175 mAh g^{-1}. To obtain cross-sectional views, samples were sliced with blades and aligned vertically. The operando cells contained a piece of $Li_4Ti_5O_{12}$ electrode (4.6 × 3.6 mm^2) and Li foil as the working and counter/reference electrodes, respectively; their preparation was carried out in the glovebox. After the sample stage had been tightly sealed, the electrolyte was injected into the cell using a syringe. The cell was discharged to 0.9 V at a rate of C/10 with an image recorded every 30 s. All potentials in this report are referenced to the Li^+/Li^0 couple.

2.4. Sample Thickness Calculation. Absorptivity can be affected by the volumetric density (ρ), thickness (t), and mass absorption coefficient (μ) of a material, as expressed by Beer's law[43]

$$I = I_0 \exp(-\mu\rho t) \quad (1)$$

where I_0 and I are the intensities of incident and transmitted X-rays, respectively. In the postedge region (at 5017 eV), the absorption coefficient of the 50% DOD sample was estimated according to the relationship $\mu = \sum_i w_i\mu_i$, where w_i and μ_i are the weight fraction and mass absorption coefficient, respectively, of the ith component. Under the assumption of uniform density throughout the electrode, the attenuation of the transmitted beam intensity (I) was highly correlated with the thickness of the electrode. To extract thickness information from the transmitted intensity, the following parameters were used, after calibration that took into account the transmittance of the Mylar films that were used seal the electrodes:[44] μ_{elec} = 368.48 cm^2/g, as estimated from the μ_i values of Li, Ti, and O at 5017 eV[45] assuming an average homogeneous composition $Li_{5.5}Ti_4O_{12}$, and ρ_{elec} = 2.09 g/cm^3, assuming 40% porosity.

2.5. Operando Optical Microscopy. A movie to obtain real-time information on the phase propagation kinetics was acquired by operando optical microscopy (see Movie S1, Supporting Information) using a lithium metal half-cell containing a piece of $Li_4Ti_5O_{12}$ electrode, sealed inside the airtight setup.

3. RESULTS

$Li_4Ti_5O_{12}$ was synthesized by a simple solid-state reaction using Li_2CO_3 and TiO_2. Characterization of the material properties, including its very low electronic conductivity, was reported in a previous work.[26] Phase purity and crystal structure were confirmed by X-ray diffraction (XRD), as shown in Figure 1a; the pattern matched an $Fd\bar{3}m$ spinel structure (JCPDS card no. 49-0207) without any notable crystalline impurities. Calendered 45-μm-thick carbon-free composite electrodes with 40% porosity were prepared to attain a specific capacity close to the

DOI: 10.1021/acs.jpcc.6b11459
J. Phys. Chem. C 2016, 120, 29030−29038

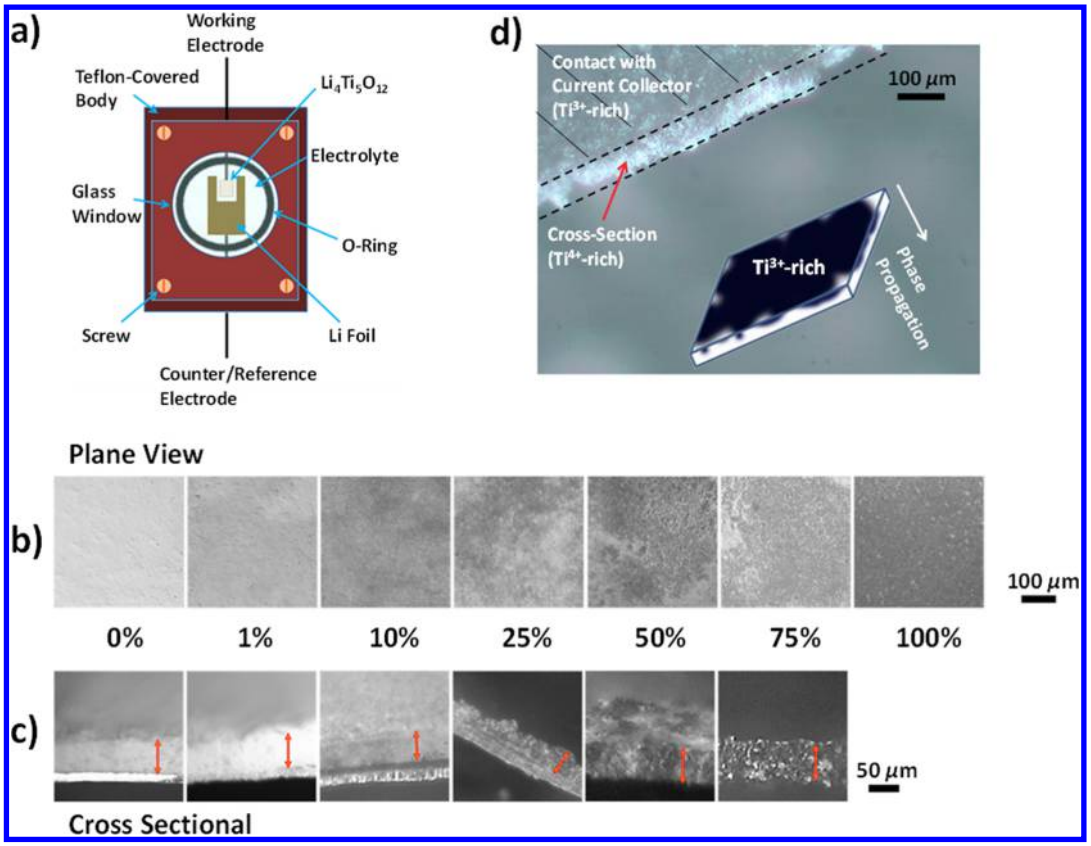

Figure 2. (a) Scheme of the airtight sample stage for optical microscopy. (b,c) Images showing (b) top surface and (c) cross-sectional views of the ex situ samples at different DODs. The red arrows in panel c indicate the thickness direction of the electrode. (d) Enlarged cross-sectional image for 25% DOD, showing dark domains propagated from the current collector side (bottom surface). The position of the current collectors is indicated by a hatch mark in panel d.

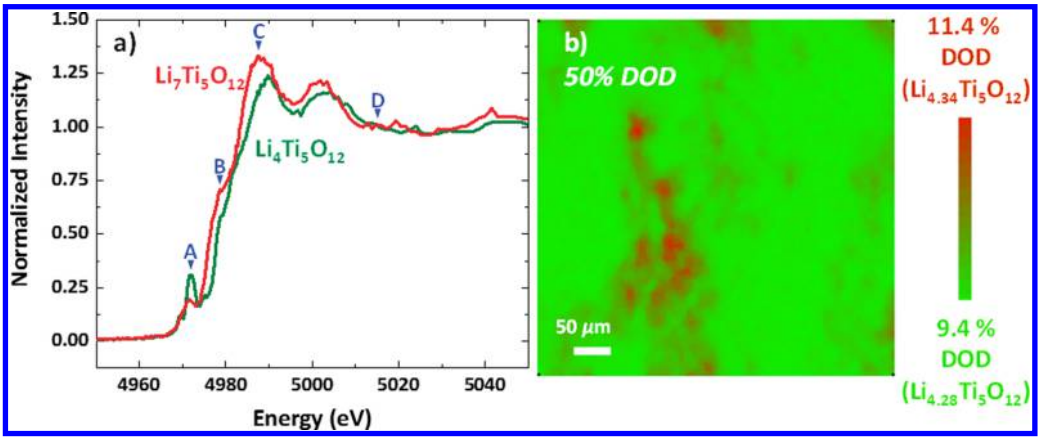

Figure 3. (a) Ti K-edge XAS spectra of $Li_4Ti_5O_{12}$ and $Li_7Ti_5O_{12}$, produced electrochemically. (b) Oxidation map of 50% DOD produced from a μ-XAS image collected in fluorescence mode. Images were taken at the energy points indicated by A−D in panel a. The first three images (at A−C) were selected to estimate the oxidation state of samples, whereas the last image (at D) was selected for normalization purposes. The green and red colors indicate the most (11.4% DOD, $Li_{\sim 4.34}Ti_5O_{12}$) and least (~9.4% DOD, $Li_{\sim 4.28}Ti_5O_{12}$) oxidized phases, respectively.

theoretical value and good durability.[26] Despite the thickness of the electrode and the absence of conducting agents, stable and extended galvanostatic cycling at a rate of $C/10$ (C = 175 mA g^{-1}, theoretical capacity) could be achieved (Figure 1b), as described in earlier reports.[25,26] $Li_4Ti_5O_{12}$ electrodes showed a clear first-order transition as a result of a two-phase reaction between $Li_4Ti_5O_{12}$ and $Li_7Ti_5O_{12}$ at 1.55 V, resulting in a specific capacity of ~170 mAh g^{-1}. The electrodes showed very little capacity loss after 30 cycles with ~100% Coulombic efficiency. Surface and cross-sectional images of the as-prepared electrodes obtained by scanning electron microscopy (SEM) revealed some lateral topological and morphological irregularities, which were due to the large sizes (up to several micrometers) and irregular shapes of the oxide particles (Figure 1c,d).

The absence of carbon in the electrodes made it possible to follow the transition between white $Li_4Ti_5O_{12}$ and dark blue $Li_7Ti_5O_{12}$ (ref 26) using visible-light digital microscopy,

DOI: 10.1021/acs.jpcc.6b11459
J. Phys. Chem. C 2016, 120, 29030−29038

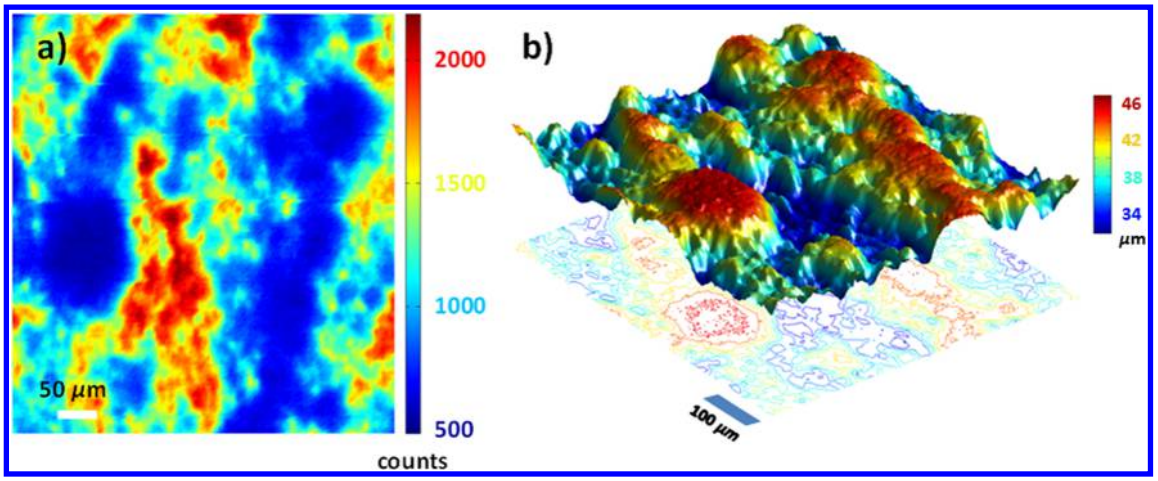

Figure 4. (a) Transmitted beam intensity in a 500 × 500 μm^2 area of the 50% DOD electrode. (b) Three-dimensional visualization of the electrode surface structure, revealing significant roughness, $R_{rms} \approx 4.41$ μm.

combined with an airtight sample stage (Figure 2a) that enabled both ex situ measurements, with samples at different depths of discharge (DOD), and operando measurements (see Experimental Section). Panels b and c of Figure 2 show images taken perpendicular to the top (i.e., opposite the current collector, Figure 1d) and the cross section, respectively, of electrodes harvested from coin cells ranging from pristine ($Li_4Ti_5O_{12}$) to 100% DOD ($Li_7Ti_5O_{12}$). In these cells, the bulk electrolyte (ion supply) and connections to the external circuit (electron supply) are located on opposite sides of the electrode (Figure 1d). In both cases, the growth of dark domains was observed as a result of the formation of Ti^{3+} as lithiation proceeded. The image of the top surface at 1% DOD showed that the whole electrode changed from white to pale blue in the early stages of lithiation. At higher reduction levels (>10% DOD samples in Figure 2b,c), dark blue domains formed rapidly, and lateral color inhomogeneity developed. The sizes of the dark domains increased upon lithiation, with the 100% DOD sample being almost completely dark blue, except for a few light speckles dispersed along the top surface. Further details on the transformation were revealed upon close inspection of the cross-section (upside-down) view of a sample harvested at 25% DOD (Figure 2d). This electrode cleanly peeled off from the current collector, revealing inhomogeneities across the thickness of the electrode. The side of the electrode originally facing the current collector (bottom fraction) was found to be mostly dark, thus indicating extensive lithiation, whereas the rest of the electrode, toward the top surface in contact with the bulk of the electrolyte in the cell, was still pale blue. As illustrated in the scheme in Figure 2d, these observations are indicative of the phase front propagating from the bottom surface (current-collector side) to the top surface (bulk-electrolyte side) of the electrode.

Complementary quantitative studies were performed by XAS at the Ti K-edge. The bulk spectra of the two end members, pristine ($Li_4Ti_5O_{12}$) and 100% DOD ($Li_7Ti_5O_{12}$), shown in Figure 3a, were used as standards to determine the compositions of mixed states. There is a 2.2 eV rising edge shift, from 4982.7 to 4980.5 eV, upon reduction of Ti^{4+} to Ti^{3+}, as measured from the first root in the first derivatives of the near-edge region. The spectra consist of three characteristic regions: pre-edge peaks at ~4971 eV, shoulder peaks at ~4976 eV, and white-line peaks at ~4987 eV, which are denoted as A, B, and C, respectively, in Figure 3a. The weak pre-edge peaks, A, are attributed to the electric quadrupole (1s → 3d transition) resulting from 3d−4p hybridization; their position and intensity are strongly related to the distortion of the centrosymmetry of the TiO_6 octahedra, which affects 3d−4p orbital mixing.[46,47] The shoulder peaks, B, are assigned to the 1s → 4p transition involving a shakedown process caused by ligand-to-metal charge transfer (LMCT), whereas the white line peaks, C, correspond to a purely dipole-allowed 1s → 4p transition without a shakedown.[48] The intensity of feature A decreased with increasing lithiation of $Li_4Ti_5O_{12}$ as a result of the decrease in structural disorder or, in other words, an increase in the centrosymmetric nature of the TiO_6 octahedra. This decreased distortion in the local structure upon lithiation is consistent with the results of previous structural studies, where $Li_7Ti_5O_{12}$, the lithiated phase, was found to show an ordered rock-salt structure.[49] Concurrently, the features in region B are more pronounced in $Li_7Ti_5O_{12}$, which indicates that the LMCT process is more prominent. The intensity in region C also increased with lithiation, indicating a decrease in 3d−4p orbital mixing due to the formation of more centrosymmetric TiO_6 octahedra, which increased the probability of the dipole transition (1s → 4p).

By virtue of the beam focusing capabilities (down to 2 × 2 μm^2), coupled with a high precision in sample positioning (±50 nm), Ti oxidation state maps were acquired. Data were obtained at four relevant energy states, denoted by arrows in Figure 3a. These states included a point in the postedge region, D, at about 5107 eV, for background normalization purposes. Because the fluorescence yield (FY) is highly localized within a probe depth of a few micrometers based on the absorption coefficient and density of the composite electrodes and measurement geometry,[50] the chemical information obtained was primarily sensitive to the top fraction of the electrode. The oxidation maps were collected perpendicular to the surface of the 50% DOD electrode in contact with the electrolyte, and the pixel-by-pixel fluorescence intensity changes with X-ray energy were fitted with a linear combination (LC) of the two standard spectra using a least-squares method (Figure 3b). The Ti oxidation map revealed a uniform, yet low level of lithiation (~$Li_{4.31}Ti_5O_{12}$) occurring near the top surface of the electrode at 50% DOD. Full spectra were also measured at the most oxidized and most reduced single pixels (Figure S1, Supporting

DOI: 10.1021/acs.jpcc.6b11459
J. Phys. Chem. C 2016, 120, 29030−29038

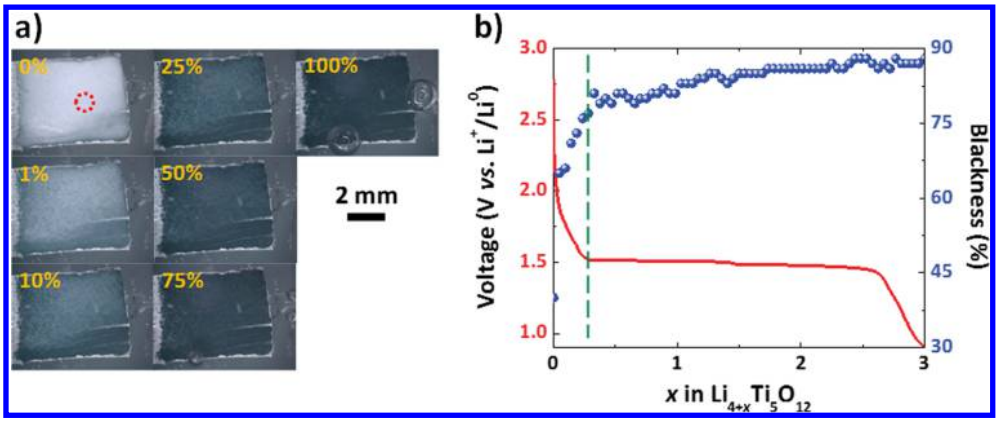

Figure 5. (a) Representative optical images taken in operando mode during discharge of $Li_4Ti_5O_{12}$ in a Li metal half-cell sealed in the holder shown in Figure 2a. (b) Voltage−capacity curve (red line) obtained in the operando experiments and degree of darkness (blue symbols), which quantifies the color change in the electrode.

Information), which resulted in compositions equivalent to ∼9.4% DOD (i.e., $Li_{\sim 4.28}Ti_5O_{12}$) and ∼11.4% DOD (i.e., $Li_{\sim 4.34}Ti_5O_{12}$), respectively. The accuracies of the LC fits are represented by the *R* factors, which were less than 1×10^{-3} in both cases (see Experimental Section). This low extent of lithiation near the top surface of the sample can be attributed to lateral and/or vertical inhomogeneities of the reaction. The field of view (FOV, 500 × 500 μm^2) was likely large enough to cover both white and dark blue domains in the optical image (50% DOD in Figure 2b). Thus, the discrepancy between the average composition of the electrode and the value measured using μ-XAS is primarily ascribed to vertical inhomogeneity due to the bottom-up mechanism of phase propagation modeled in Figure 2c.

The discrepancy between the lateral inhomogeneity observed by optical microscopy (Figure 2b) and the homogeneity of the oxidation states in the μ-XAS map (Figure 3b) of the top fraction of the electrode, exposed to the electrolyte, at 50% DOD can be attributed to the different optical skin depths of the techniques, which can be generated by the morphology and topology of the architecture. In other words, dark Ti^{3+}-rich domains close to the current collector could be visible in an optical image taken from the surface facing the bulk electrolyte, as in Figure 2b, if covered by lightly colored Ti^{3+}-poor domains, because of the transparency of the latter. This situation appears to have applied to the 50% DOD sample. This complex phase distribution vis-à-vis the topology of the electrode can be evaluated from the response of the sample to the X-ray beam. Indeed, the intensity of the beam transmitted at 5017 eV through the 50% DOD sample during XAS measurements fluctuated noticeably, as shown in Figure 4a, which corresponds to the same area as in Figure 3b. Because the image was collected well above the absorption edge, this attenuation is correlated with the absorptivity of the sample, regardless of the chemical state. The average thickness derived from the transmitted beam intensity was estimated to be ∼40 μm, which matches well with the actual thickness based on the SEM results in Figure 1d. To account for the compositional heterogeneity, a model was built in which the composition of the bottom half (i.e., ∼20 μm) was $Li_7Ti_5O_{12}$, with the rest being a composition close to the pristine state. The corrected mass coefficients ($\mu_{Li_4Ti_5O_{12}}$ = 376.62 cm^2/g and $\mu_{Li_7Ti_5O_{12}}$ = 360.35 cm^2/g) were again applied for each pixel (see eq 1 in the Experimental Section). The resulting electrode topology is shown in Figure 4b. The electrode revealed a lateral microstructural inhomogenity with a root-mean-square roughness (R_{rms}) of ∼4.41 μm. Indeed, thinner portions of the electrode corresponded to slightly higher values of lithiation.

Real-time information concerning the kinetics of the phase propagation was acquired by operando optical microscopy (see Figure 5) using a half-cell containing a $Li_4Ti_5O_{12}$ electrode and a lithium foil counter electrode, sealed inside the airtight sample stage (Figure 2a). A movie obtained from the operando cell showing the color changes can be found in the Supporting Information (Movie S1). Optical images at relevant DOD states were extracted from the complete image set, as presented in Figure 5a. The resulting voltage−composition trace is shown in Figure 5b. The electrochemical signals from the operando cell were close to those obtained in standard coin cells (Figure 1b), with the electrode achieving full capacity (3 mol of Li in $Li_4Ti_5O_{12}$) at the 0.9 V discharge cutoff. To obtain detailed insight, the degree of darkness was quantified for the region marked with a circle in the 0% DOD image and is plotted with the voltage curve in Figure 5b. The area was carefully chosen to be representative of the phase propagation in the whole electrode, where inhomogeneity seemed to be minimized. The color change demonstrated a strong correlation with the electrochemical response. The largest color change took place in the very early stages of lithiation (up to ∼10% DOD; see the dashed line in Figure 5b), indicating the formation of mixed states of Ti^{3+}/Ti^{4+} up to the surface, which resulted in a sharp increase in electronic conductivity. Electronic percolation throughout the electrode was thus rapidly achieved as the voltage dropped from the open-circuit voltage (∼2.77 V) to 1.5 V. Upon completion of electronic percolation throughout the electrode, phase propagation from the current-collector side to the electrolyte side occurred. During phase propagation, the color of the electrode became only slightly darker, with subtle changes observed after intercalation of 1.5 mol of Li^+ (50% DOD). Finally, the darkest color was achieved at 0.9 V, although, as in the case of the ex situ experiments, some lighter speckles were still observed. Bubbling was observed during the reduction of $Li_4Ti_5O_{12}$. It is possible that this phenomenon is related to the macroscopic observations of gassing during operation of these electrodes in large format cells,[51−54] the origin of which is still under debate.

DOI: 10.1021/acs.jpcc.6b11459
J. Phys. Chem. C 2016, 120, 29030−29038

4. DISCUSSION

The inhomogeneities in the degree of lithiation observed both ex situ and operando in electrodes that were discharged slowly (C/10) are at odds with a mechanism in which only a solid solution between end members is formed[28] because the transformation of such a solid solution would involve homogeneity in chemical states throughout the electrode states, especially in equilibrated, ex situ samples. Overall, the results confirm that lithiated, Ti^{3+}-rich phases propagate through the thick composite electrode in the very early stages of reaction (~1% DOD), which is very rapidly followed by the uneven advance of darker phases toward the whole electrode structure. Thus, these results are in agreement with the phase progression proposed on the basis of Raman and impedance spectroscopy.[26] The first wave of lithiation in carbon-free $Li_4Ti_5O_{12}$ involves the formation of percolating domains with high electronic conductivity, thus enabling the complete lithiation of the electrode. This initial process can be viewed as introducing an electronically conductive additive in situ, which significant levels of percolation achieved with only 1% of electronically conducting phase. Recently, the formation of percolation channels within individual grains was identified to play a role in the early propagation of lithiated domains in thin (<1-μm) films of $Li_4Ti_5O_{12}$.[31] Particle-by-particle reactions have also been proposed by others for $Li_4Ti_5O_{12}$ aggregates based on data from scanning transmission electron microscopy-electron energy loss spectroscopy (STEM-EELS).[55] This percolation appears to be sufficiently fast to occur throughout a structure that is more than 40 times thicker. Growth of the lithiated domains from these channels could lead to the lateral inhomogeneities observed at intermediate depths of discharge.

Initially, the electrochemical reaction is hindered by the poor electronic and ionic conduction in $Li_4Ti_5O_{12}$.[27,30] Once the lithiated phases percolate in the electrode, both electronic conduction[27] and ionic conduction[30] are significantly boosted. It is remarkable that such boosts can be accomplished with just 1% conductive phase. Achieving functional battery electrodes containing only 1% of conductive additives would be highly desirable as a step toward the increases in energy density at the cell level required for the widespread penetration of battery-powered vehicles. Therefore, the study of this type of architecture should provide lessons that can be translated to materials that cannot be studied by optical microscopy because of the absence of color changes during the reaction. It is not possible to determine whether this early homogeneous state is due to the presence of some miscibility of Li in $Li_4Ti_5O_{12}$, possibly in a metastable state,[31] before a second phase forms because the data collected in this study provided limited structural insight. The fact that, beyond the initial percolating step, lithiation is more predominant close to the current collector strongly suggests that electron conduction remains slower than ionic conduction in the absence of conducting additives, especially at particle boundaries. Composite electrodes can easily develop morphological inhomogenities in their structures as a result of the presence of multiple interfaces among multiple components,[56] thus leading to compositional gradients and multiple domains. The transport limitations highlighted here are in contrast to reports on $LiFePO_4$ electrodes containing large amounts of carbon.[33] In the presence of these large amounts of carbon, ionic transport became limiting at high rates of charging, so that the most reacted domains were observed in proximity to the electrolyte, as opposed to the current collector.

5. CONCLUSIONS

A systematic study of the phase propagation in carbon-free $Li_4Ti_5O_{12}$ composite electrodes has been presented. Through the combination of data from optical microscopy and μ-XAS, initial lithiation was observed to occur throughout the electrode in the early stages of the reaction, followed by bulk lithiation starting with regions in closest contact with the current collector and progressing toward regions in contact with the bulk electrode. This latter observation suggests that the reaction is still somewhat sluggish even in the presence of the electronic carriers throughout the electrode, possibly due to the fact that not all particles equally react or have good electrical contacts. This contact inhomogeneity is also likely to occur in electrodes made with very small amounts of conductive additives, regardless of the active material. Lateral optical (color) inhomogenity was also noticed in the electrodes and could be ascribed to local gradients in interparticle contacts and/or in thickness of the electrode. Our results are consistent with theories of preferential lithiation, of which the particle-by-particle model would be the extreme expression. However, it is not yet possible to determine whether the behavior is imposed by kinetic (e.g., diffusion, contacts) or thermodynamic parameters. The results highlight that morphological or chemical modifications of the particles so that the initial lithiation is facile could be effective in obtaining high rate performance in the composite electrode, as they would favor the formation of percolating highly conductive networks. This design would benefit from further details on the relationships between phase propagation and crystallographic orientation. Broadly speaking, this study highlights the importance of understanding reaction mechanisms at the level of realistic particle architectures, especially in devices, such as batteries, in which energy density directly scales with electrode thickness. Simple optical microscopy or advanced techniques based on X-ray microbeams have been demonstrated here to be of great value for these meso- and macroscale phenomena to be revealed.

■ ASSOCIATED CONTENT

Supporting Information

The Supporting Information is available free of charge on the ACS Publications website at DOI: 10.1021/acs.jpcc.6b11459.

Single-pixel Ti K-edge XAS spectra extracted at the most oxidized and reduced points of the 50% DOD sample (PDF)

Movie collected during operando optical microscopy (AVI)

■ AUTHOR INFORMATION

Corresponding Author

*E-mail: jcabana@uic.edu. Phone: 312-355-4309.

ORCID

Jordi Cabana: 0000-0002-2353-5986

Present Addresses

§C.K.: Department of Materials Science and Engineering, Chungnam National University, Daejeon, 34134, Korea.

⊥Y.-S.Y.: Advanced Light Source, Lawrence Berkeley National Laboratory, Berkeley, CA 94720.

DOI: 10.1021/acs.jpcc.6b11459
J. Phys. Chem. C 2016, 120, 29030−29038

Author Contributions

[‖]C.K. and Y.-S.Y. contributed equally to this work.

Notes

The authors declare no competing financial interest.

■ ACKNOWLEDGMENTS

This work was supported by the Assistant Secretary for Energy Efficiency and Renewable Energy, Office of Vehicle Technologies, of the U.S. Department of Energy under Contract DE-AC02-05CH11231. Y.-S.Y. was supported as part of the NorthEast Center for Chemical Energy Storage, an Energy Frontier Research Center funded by the U.S. Department of Energy, Office of Science, Office of Basic Energy Sciences, under Award DE-SC0012583.

■ REFERENCES

(1) Goodenough, J. B. Evolution of Strategies for Modern Rechargeable Batteries. *Acc. Chem. Res.* **2013**, *46*, 1053−1061.
(2) Armand, M.; Tarascon, J. M. Building Better Batteries. *Nature* **2008**, *451*, 652−657.
(3) Dunn, B.; Kamath, H.; Tarascon, J. M. Electrical Energy Storage for the Grid: A Battery of Choices. *Science* **2011**, *334*, 928−935.
(4) Thackeray, M. M.; Wolverton, C.; Isaacs, E. D. Electrical Energy Storage for Transportation—Approaching the Limits of, and Going beyond, Lithium-Ion Batteries. *Energy Environ. Sci.* **2012**, *5*, 7854−7863.
(5) Peng, Z.; Freunberger, S. A.; Chen, Y.; Bruce, P. G. A Reversible and Higher-Rate Li-O_2 Battery. *Science* **2012**, *337*, 563−566.
(6) Slater, M. D.; Kim, D.; Lee, E.; Johnson, C. S. Sodium-Ion Batteries. *Adv. Funct. Mater.* **2013**, *23*, 947−958.
(7) Armstrong, A. R.; Lyness, C.; Panchmatia, P. M.; Islam, M. S.; Bruce, P. G. The Lithium Intercalation Process in the Low-Voltage Lithium Battery Anode $Li_{1+x}V_{1-x}O_2$. *Nat. Mater.* **2011**, *10*, 223−229.
(8) Poizot, P.; Laruelle, S.; Grugeon, S.; Dupont, L.; Tarascon, J. M. Nano-Sized Transition-Metal Oxides as Negative-Electrode Materials for Lithium-Lon Batteries. *Nature* **2000**, *407*, 496−499.
(9) Vaughey, J. T.; Kepler, K.; Johnson, C. S.; Sarakonsri, T.; Benedek, R.; O'Hara, J.; Hackney, S.; Thackeray, M. M. Intermetallic Insertion Electrodes for Lithium Batteries. In *Intercalation Compounds for Battery Materials: Proceedings of the International Symposium*; Nazzi, G., Thackeray, M., Ohzuku, T., Eds.; The Electrochemical Society: Pennington, NJ, 2000; Vol. *99-24*; pp 280−289.
(10) Whittingham, M. S. Lithium Batteries and Cathode Materials. *Chem. Rev.* **2004**, *104*, 4271−4302.
(11) Liu, G.; Zheng, H.; Simens, A. S.; Minor, A. M.; Song, X.; Battaglia, V. S. Optimization of Acetylene Black Conductive Additive and PVDF Composition for High-Power Rechargeable Lithium-Ion Cells. *J. Electrochem. Soc.* **2007**, *154*, A1129−A1134.
(12) Kang, B.; Ceder, G. Battery Materials for Ultrafast Charging and Discharging. *Nature* **2009**, *458*, 190−193.
(13) Mohanty, D.; Li, J.; Born, R.; Maxey, L. C.; Dinwiddie, R. B.; Daniel, C.; Wood, D. L., III. Non-Destructive Evaluation of Slot-Die-Coated Lithium Secondary Battery Electrodes by In-Line Laser Caliper and IR Thermography Methods. *Anal. Methods* **2014**, *6*, 674−683.
(14) Chen, Y. H.; Wang, C. W.; Zhang, X.; Sastry, A. M. Porous Cathode Optimization for Lithium Cells: Ionic and Electronic Conductivity, Capacity, and Selection of Materials. *J. Power Sources* **2010**, *195*, 2851−2862.
(15) Deng, D.; Kim, M. G.; Lee, J. Y.; Cho, J. Green Energy Storage Materials: Nanostructured TiO_2 and Sn-Based Anodes for Lithium-Ion Batteries. *Energy Environ. Sci.* **2009**, *2*, 818−837.
(16) Kavan, L. Electrochemistry of Titanium Dioxide: Some Aspects and Highlights. *Chem. Rec.* **2012**, *12*, 131−142.
(17) Wagemaker, M.; Mulder, F. M. Properties and Promises of Nanosized Insertion Materials for Li-Ion Batteries. *Acc. Chem. Res.* **2013**, *46*, 1206−1215.
(18) Ohzuku, T.; Ueda, A.; Yamamoto, N. Zero-Strain Insertion Material of $Li[Li_{1/3}Ti_{5/3}]O_4$ for Rechargeable Lithium Cells. *J. Electrochem. Soc.* **1995**, *142*, 1431−1435.
(19) Ferg, E.; Gummow, R. J.; de Kock, A.; Thackeray, M. M. Spinel Anodes for Lithium-Ion Batteries. *J. Electrochem. Soc.* **1994**, *141*, L147−L150.
(20) Wagemaker, M.; van Eck, E. R. H.; Kentgens, A. P. M.; Mulder, F. M. Li-Ion Diffusion in the Equilibrium Nanomorphology of Spinel $Li_{4+x}Ti_5O_{12}$. *J. Phys. Chem. B* **2009**, *113*, 224−230.
(21) Wagemaker, M.; Simon, D. R.; Kelder, E. M.; Schoonman, J.; Ringpfeil, C.; Haake, U.; Lützenkirchen-Hecht, D.; Frahm, R.; Mulder, F. M. A Kinetic Two-Phase and Equilibrium Solid Solution in Spinel $Li_{4+x}Ti_5O_{12}$. *Adv. Mater.* **2006**, *18*, 3169−3173.
(22) Pang, W. K.; Peterson, V. K.; Sharma, N.; Shiu, J.-J.; Wu, S.-H. Lithium Migration in $Li_4Ti_5O_{12}$ Studied Using in Situ Neutron Powder Diffraction. *Chem. Mater.* **2014**, *26*, 2318−2326.
(23) Hao, X.; Bartlett, B. M. $Li_4Ti_5O_{12}$ Nanocrystals Synthesized by Carbon Templating from Solution Precursors Yield High Performance Thin Film Li-Ion Battery Electrodes. *Adv. Energy Mater.* **2013**, *3*, 753−761.
(24) Prakash, A. S.; Manikandan, P.; Ramesha, K.; Sathiya, M.; Tarascon, J. M.; Shukla, A. K. Solution-Combustion Synthesized Nanocrystalline $Li_4Ti_5O_{12}$ As High-Rate Performance Li-Ion Battery Anode. *Chem. Mater.* **2010**, *22*, 2857−2863.
(25) Song, M.-S.; Benayad, A.; Choi, Y.-M.; Park, K.-S. Does $Li_4Ti_5O_{12}$ Need Carbon in Lithium Ion Batteries? Carbon-Free Electrode with Exceptionally High Electrode Capacity. *Chem. Commun.* **2012**, *48*, 516−518.
(26) Kim, C.; Norberg, N. S.; Alexander, C. T.; Kostecki, R.; Cabana, J. Mechanism of Phase Propagation During Lithiation in Carbon-Free $Li_4Ti_5O_{12}$ Battery Electrodes. *Adv. Funct. Mater.* **2013**, *23*, 1214−1222.
(27) Young, D.; Ransil, A.; Amin, R.; Li, Z.; Chiang, Y.-M. Electronic Conductivity in the $Li_{4/3}Ti_{5/3}O_4$−$Li_{7/3}Ti_{5/3}O_4$ System and Variation with State-of-Charge as a Li Battery Anode. *Adv. Energy Mater.* **2013**, *3*, 1125−1129.
(28) Kim, C.; Buonsanti, R.; Yaylian, R.; Milliron, D. J.; Cabana, J. Carbon-Free TiO_2 Battery Electrodes Enabled by Morphological Control at the Nanoscale. *Adv. Energy Mater.* **2013**, *3*, 1286−1291.
(29) Alexander, C. T.; Kim, C.; Yaylian, R.; Cabana, J. Toward General Rules for the Design of Battery Electrodes Based on Titanium Oxides and Free of Conductive Additives. *Energy Technol.* **2014**, *2*, 383−390.
(30) Schmidt, W.; Bottke, P.; Sternad, M.; Gollob, P.; Hennige, V.; Wilkening, M. Small Change—Great Effect: Steep Increase of Li Ion Dynamics in $Li_4Ti_5O_{12}$ at the Early Stages of Chemical Li Insertion. *Chem. Mater.* **2015**, *27*, 1740−1750.
(31) Verde, M. G.; Baggetto, L.; Balke, N.; Veith, G. M.; Seo, J. K.; Wang, Z.; Meng, Y. S. Elucidating the Phase Transformation of $Li_4Ti_5O_{12}$ Lithiation at the Nanoscale. *ACS Nano* **2016**, *10*, 4312−4321.
(32) Nanda, J.; Remillard, J.; O'Neill, A.; Bernardi, D.; Ro, T.; Nietering, K. E.; Go, J.-Y.; Miller, T. J. Local State-of-Charge Mapping of Lithium-Ion Battery Electrodes. *Adv. Funct. Mater.* **2011**, *21*, 3282−3290.
(33) Liang, G.; Croft, M. C.; Zhong, Z. Energy Dispersive X-ray Diffraction Profiling of Prototype $LiMn_2O_4$-Based Coin Cells. *J. Electrochem. Soc.* **2013**, *160*, A1299−1303.
(34) Liu, J.; Kunz, M.; Chen, K.; Tamura, N.; Richardson, T. J. Visualization of Charge Distribution in a Lithium Battery Electrode. *J. Phys. Chem. Lett.* **2010**, *1*, 2120−2123.
(35) Harris, S. J.; Timmons, A.; Baker, D. R.; Monroe, C. Direct *In Situ* Measurements of Li Transport in Li-Ion Battery Negative Electrodes. *Chem. Phys. Lett.* **2010**, *485*, 265−274.
(36) Pfanzelt, M.; Kubiak, P.; Fleischhammer, M.; Wohlfahrt-Mehrens, M. TiO_2 Rutile—An Alternative Anode Material for Safe Lithium-Ion Batteries. *J. Power Sources* **2011**, *196*, 6815−6821.
(37) Robert, R.; Zeng, D.; Lanzirotti, A.; Adamson, P.; Clarke, S. J.; Grey, C. P. Scanning X-ray Fluorescence Imaging Study of Lithium

DOI: 10.1021/acs.jpcc.6b11459
J. Phys. Chem. C 2016, 120, 29030−29038

Insertion into Copper Based Oxysulfides for Li-Ion Batteries. *Chem. Mater.* **2012**, *24*, 2684−2691.
(38) Ouvrard, G.; Zerrouki, M.; Soudan, P.; Lestriez, B.; Masquelier, C.; Morcrette, M.; Hamelet, S.; Belin, S.; Flank, A. M.; Baudelet, F. Heterogeneous Behaviour of the Lithium Battery Composite Electrode $LiFePO_4$. *J. Power Sources* **2013**, *229*, 16−21.
(39) Tanida, H.; Yamashige, H.; Orikasa, Y.; Fujimoto, T.; Oishi, M.; Murayama, H.; Arai, H.; Katayama, M.; Inada, Y.; Ohta, T.; et al. *In Situ* Two-Dimensional Micro-Imaging XAFS with CCD Detector. *J. Phys.: Conf. Ser.* **2013**, *430*, 012021.
(40) Kirkpatrick, P.; Baez, A. V. Formation of Optical Images by X-Rays. *J. Opt. Soc. Am.* **1948**, *38*, 766−774.
(41) Webb, S. M. SIXpack: A Graphical User Interface for XAS Analysis Using IFEFFIT. *Phys. Scr.* **2005**, *2005*, 1011−1014.
(42) Webb, S. M. The MicroAnalysis Toolkit: X-ray Fluorescence Image Processing Software. In *Proceedings of the 10th International Conference on X-ray Microscopy*; McNulty, I., Eyberger, C., Lai, B., Eds.; American Institute of Physics: College Park, MD, 2011; Vol. *1365*, pp 196−199.
(43) Thompson, A. C.; Attwood, D. T.; Gullikson, E. M.; Howells, M. R.; Kim, K.-J.; Kirz, J.; Kortright, J. B.; Lindau, I.; Liu, Y.; Pianetta, P.; Robinson, A. L.; Scofield, J.; Underwood, J.; Williams, G.; Winick, H. *X-ray Data Booklet*; Lawrence Berkeley National Laboratory, University of California: Berkeley, CA, 2009.
(44) Henke, B. L.; Gullikson, E. M.; Davis, J. C. X-ray Interactions: Photoabsorption, Scattering, Transmission, and Reflection at E = 50−30,000 eV, Z = 1−92. *At. Data Nucl. Data Tables* **1993**, *54*, 181−342.
(45) Seltzer, S. M. Calculation of Photon Mass Energy-Transfer and Mass Energy-Absorption Coefficients. *Radiat. Res.* **1993**, *136*, 147−170.
(46) Farges, F.; Brown, G. E., Jr.; Rehr, J. J. Ti K-edge XANES Studies of Ti Coordination and Disorder in Oxide Compounds: Comparison between Theory and Experiment. *Phys. Rev. B: Condens. Matter Mater. Phys.* **1997**, *56*, 1809.
(47) Ra, W.; Nakayama, M.; Cho, W.; Wakihara, M.; Uchimoto, Y. Electronic and Local Structural Changes in $Li_{2+x}Ti_3O_7$ Ramsdellite Compounds upon Electrochemical Li-Ion Insertion Reactions by X-Ray Absorption Spectroscopy. *Phys. Chem. Chem. Phys.* **2006**, *8*, 882−889.
(48) Song, H.; Yun, S.-W.; Chun, H.-H.; Kim, M.-G.; Chung, K. Y.; Kim, H. S.; Cho, B.-W.; Kim, Y.-T. Anomalous Decrease in Structural Disorder due to Charge Redistribution in Cr-Doped $Li_4Ti_5O_{12}$ Negative-Electrode Materials for High-Rate Li-Ion Batteries. *Energy Environ. Sci.* **2012**, *5*, 9903−9913.
(49) Ariyoshi, K.; Yamato, R.; Ohzuku, T. Zero-Strain Insertion Mechanism of $Li[Li_{1/3}Ti_{5/3}]O_4$ for Advanced Lithium-Ion (Shuttlecock) Batteries. *Electrochim. Acta* **2005**, *51*, 1125−1129.
(50) Tröger, L.; Arvanitis, D.; Baberschke, K.; Michaelis, H.; Grimm, U.; Zschech, E. Full Correction of the Self-Absorption in Soft-Fluorescence Extended X-Ray-Absorption Fine Structure. *Phys. Rev. B: Condens. Matter Mater. Phys.* **1992**, *46*, 3283.
(51) He, M.; Castel, E.; Laumann, A.; Nuspl, G.; Novák, P.; Berg, E. J. In Situ Gas Analysis of $Li_4Ti_5O_{12}$ Based Electrodes at Elevated Temperatures. *J. Electrochem. Soc.* **2015**, *162*, A870−A876.
(52) He, Y.-B.; Li, B.; Liu, M.; Zhang, C.; Lv, W.; Yang, C.; Li, J.; Du, H.; Zhang, B.; Yang, Q.-H.; Kim, J.-K.; Kang, F. Gassing in $Li_4Ti_5O_{12}$-Based Batteries and Its Remedy. *Sci. Rep.* **2012**, *2*, 913.
(53) Belharouak, I.; Koenig, G. M., Jr.; Tan, T.; Yumoto, H.; Ota, N.; Amine, K. Performance Degradation and Gassing of $Li_4Ti_5O_{12}$/$LiMn_2O_4$ Lithium-Ion Cells. *J. Electrochem. Soc.* **2012**, *159*, A1165−A1170.
(54) Bernhard, R.; Meini, S.; Gasteiger, H. A. On-Line Electrochemical Mass Spectrometry Investigations on the Gassing Behavior of $Li_4Ti_5O_{12}$ Electrodes and Its Origins. *J. Electrochem. Soc.* **2014**, *161*, A497−A505.
(55) Kitta, M.; Akita, T.; Tanaka, S.; Kohyama, M. Characterization of Two Phase Distribution in Electrochemically-Lithiated Spinel $Li_4Ti_5O_{12}$ Secondary Particles by Electron Energy-Loss Spectroscopy. *J. Power Sources* **2013**, *237*, 26−32.
(56) Harris, S. J.; Lu, P. Effects of Inhomogeneities—Nanoscale to Mesoscale—on the Durability of Li-Ion Batteries. *J. Phys. Chem. C* **2013**, *117*, 6481−6492.

DOI: 10.1021/acs.jpcc.6b11459
J. Phys. Chem. C 2016, 120, 29030−29038